Biophysical Journal
Review

Biophysical Society

Single-molecule counting applied to the study of GPCR oligomerization

Joshua N. Milstein,[1,2,*] Daniel F. Nino,[2] Xiaohan Zhou,[1,2] and Claudiu C. Gradinaru[1,2,*]
[1]Department of Physics, University of Toronto, Toronto, Ontario, Canada and [2]Department of Chemical and Physical Sciences, University of Toronto Mississauga, Mississauga, Ontario, Canada

ABSTRACT Single-molecule counting techniques enable a precise determination of the intracellular abundance and stoichiometry of proteins and macromolecular complexes. These details are often challenging to quantitatively assess yet are essential for our understanding of cellular function. Consider G-protein-coupled receptors—an expansive class of transmembrane signaling proteins that participate in many vital physiological functions making them a popular target for drug development. While early evidence for the role of oligomerization in receptor signaling came from ensemble biochemical and biophysical assays, innovations in single-molecule measurements are now driving a paradigm shift in our understanding of its relevance. Here, we review recent developments in single-molecule counting with a focus on photobleaching step counting and the emerging technique of quantitative single-molecule localization microscopy—with a particular emphasis on the potential for these techniques to advance our understanding of the role of oligomerization in G-protein-coupled receptor signaling.

INTRODUCTION

Many cellular pathways are regulated by proteins that form into quaternary complexes. Being able to determine the composition, structural organization, and dynamics of these macromolecular protein complexes is essential to understanding biological function (1,2). For example, protein stoichiometry is a critical modulator of biological processes from stem cell division (3), to viral entry by HIV during infection (4), to signal initiation by G-protein-coupled receptors (GPCRs). GPCRs provide a powerful example of the need to develop better tools for measuring protein stoichiometry. GPCRs are membrane proteins involved in nearly every facet of signaling, which play a key role in a myriad of physiological responses including visual, olfactory, pheromone, and taste response, while providing regulatory control in neuronal and hormonal signaling and cell homeostasis (5,6). Around 700 FDA-approved drugs (∼35% of the total drug market) target GPCRs, but since only ∼12% of GPCRs have been subjected to large-scale drug screens, they hold tremendous untapped pharmacological potential (7). Despite at least two decades of intense study, whether these receptors or their associated G proteins assemble into oligomeric complexes, and the functional importance of these dynamic complexes, remains highly controversial (8–10). However, in recent years, advances in single-molecule imaging have begun to reveal the importance of the macromolecular organization and dynamics of GPCRs for controlling signaling outputs.

Signaling occurs when a ligand (agonist), binding at the extracellular surface of a GPCR, induces long-range conformational changes in the receptor, which in turn activate the G protein (11). However, the GPCR response is complicated by oligomerization of both receptors and G proteins and by involvement in multiple signal pathways with varying efficacy in different environments. According to the prevalent model, a monomeric receptor couples to a monomeric G protein in a process promoted by the agonist ligand (12). However, a different view has emerged in recent years that many GPCRs form transient or stable homo- or hetero-oligomers and that those oligomers have a physiological role (13–15). Attempts to estimate the size of GPCR oligomers in live cells identified a variety of species, including monomers, transient dimers, stable dimers, and stable tetramers. The identity of receptors, the expression level, and the evaluation method are all partly responsible for this lack of consensus.

A multitude of single-molecule fluorescence (SMF) imaging and spectroscopy techniques have emerged in the past three decades to study the structure, dynamics, and interactions of biological macromolecules (16–18). Here, we review recent advances in SMF counting with an emphasis on photobleaching step counting (PSC) and quantitative

Submitted May 31, 2022, and accepted for publication July 28, 2022.
*Correspondence: josh.milstein@utoronto.ca or claudiu.gradinaru@utoronto.ca
Editor: Meyer B. Jackson.
https://doi.org/10.1016/j.bpj.2022.07.034

single-molecule localization microscopy (qSMLM). We then focus on studies applying modern single-molecule counting methods to quantitatively characterize the distribution of oligomeric species of various GPCRs. While most of these single-molecule studies were performed *in vitro* on detergent-purified samples, several recent studies were able to successfully track the spatiotemporal oligomerization behavior of GPCRs in live cells.

PSC

Among various SMF techniques, PSC is an intuitive and direct way to investigate the stoichiometry of oligomeric complexes. Photobleaching is the cessation of emission of a fluorophore after a certain time, often seconds to minutes, under continuous excitation. This is due to an irreversible chemical transition to a non-fluorescent species caused by singlet oxygen and free radicals in solution. While photobleaching is typically something one tries to mitigate (19), in PSC applications, photobleaching is utilized to estimate the number of fluorophores that contribute to an intensity trace recorded from an individual spot/particle in the image. Assuming perfect one-to-one labeling efficiency, the number of fluorophores estimated by PSC equals the number of units in an oligomer formed by the protein of interest. Furthermore, PSC can resolve fluorophore localizations separated by distances as small as 10 nm, with a precision on the order of 5 nm (20). Thus, PSC analysis can provide both the number of subunits and their spatial arrangement within protein oligomers (assuming individual oligomers can be spatially resolved).

While the basic idea behind PSC is straightforward (i.e., simply counting the number of downward steps in an intensity trace from a single spot in the image), there are various technical hurdles to obtaining accurate counts. As shown in Fig. 1 *C*, the fluorescence intensity in a typical trace exhibits fluctuations due to photon shot noise and to camera offset and readout noise. The key aspect of the analysis is to identify photobleaching events through the timing and the size of the intensity drops. The most direct way to analyze an intensity trace is through visual inspection, which requires manually investigating each individual trace (21,22). Applying edge-preserving signal filtering, such as the Chung-Kennedy filter, can clean up noisy intensity traces and facilitate manual estimates of photobleaching steps (23,24). However, while this yields accurate results for traces with a limited number of steps (e.g., <10), as the number of fluorophores contributing to a single trace increase, the process becomes time consuming, and the results are biased by undercounting.

A more accurate and automated approach, which was previously applied in the Gradinaru lab, employs change-point (CP) analysis (25). The method involves calculating the cumulative sum of the signal and then identifying change points at the time points where the slope varies. By applying a Student's *t*-test to examine slope changes, the change points are automatically detected and stored (Fig. 2 *A*). This enables an extraction of the number of photobleaching steps N_{st}, the stepwise photobleaching intensities I_{st}, and the photobleaching times τ_{pb} from each trace. Given the incomplete labeling and the stochastic nature of excitation and photobleaching, the distribution of N_{st} over many ($\sim 10^3$) individual particles can be best described by a binomial distribution (Fig. 2 *B*), where the maximum number of steps n reflects the oligomeric size and the probability p corresponds to the probability of detecting a fluorophore in a multi-labelled oligomeric particle (26). The distributions of step intensities I_{st} (Fig. 2 *C*) and of photobleaching times τ_{pb} can be used to filter out impurities and/or sub-stochiometric intensity changes.

In recent years, new Bayesian (27), machine-learning (28), or a combination of both (29) approaches have been developed to improve the precision and robustness of PSC data analysis. Recently, we used a Bayesian-based method to analyze PSC data that incorporates the mean fluorophore brightness and Poisson shot noise as priors. With the additional information provided by these physics-based priors, we are able to optimize our estimate of the initial number of fluorophores by finding the maximum *a posteriori* probability (MAP) of the number of photobleaching steps in a

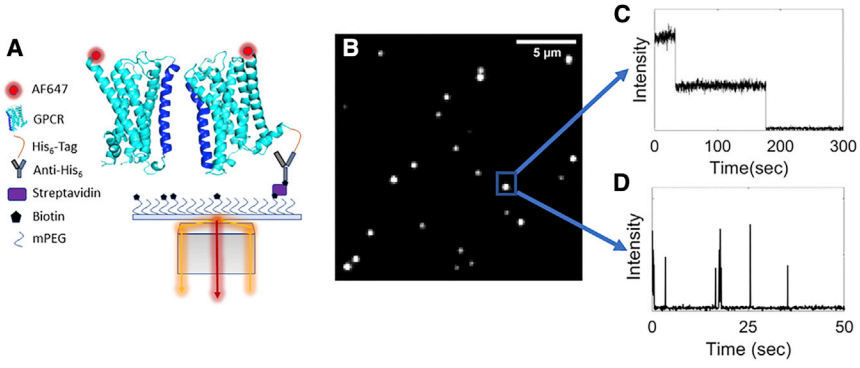

FIGURE 1 Surface immobilization of a GPCR dimer with typical intensity traces. (*A*) Single Alexa Fluor 647-labeled GPCRs (a dimer is shown in the *illustration* [*blue*: dimer interface]) were attached to a sparsely biotinylated PEG surface successively layered with streptavidin and biotinylated anti-His antibody, then imaged via TIRF microscopy at 638 nm. (*B*) TIRF image of surface immobilized, fluorescently labeled GPCRs. (*C*) Intensity trace of a GPCR dimer used for PSC analysis obtained in 2 mM Trolox and GODCAT (100 nM glucose oxidase, 1.5 µM catalase, 56 mM glucose) antifade buffer. (*D*) Intensity trace of a GPCR dimer used for qSMLM analysis imaged in 10 mM MEA/50mM BME to induce blinking and a 13 mM PCA/50 nM PCD oxygen scavenging system to reduce photobleaching. To see this figure in color, go online.

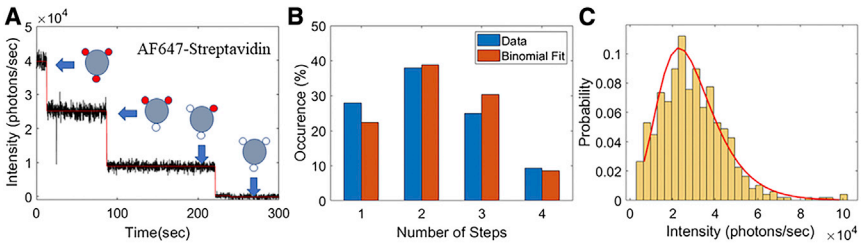

FIGURE 2 Photobleach step-counting analysis. (*A*) Intensity time trace (*black line*) from an Alexa Fluor 647-conjugated streptavidin molecule analyzed according to a change-point algorithm to identify photobleaching steps (*red lines*). Three steps were detected for this trace. (*B*) Data from 161 complexes in a sample were used to build a histogram of the number of photobleaching steps per complex (*blue*), which was fit to a binomial distribution (*red*) to acquire the maximum number of steps n and the probability to detect a single fluorophore p ($n = 4$ and $p = 0.54$ in this case). (*C*) The values of the intensity drops for all detected photobleaching steps were used to build a histogram of stepwise intensity (*yellow*), which can be fit to a generalized extreme value distribution (*red line*) to acquire the mean and standard deviation of intensity values for a single fluorophore molecule. To see this figure in color, go online.

given data trace. This yields a simple, reliable, and computationally efficient method for extracting accurate counts from PSC data (30). Comparison of CP and MAP methods on both simulated data and experimental data from a (short) standard DNA ladder construct yielded similar results (30). However, the MAP analysis can reliably estimate the number of steps/fluorophores in a single trace up to $N_{st} \sim 100$, while the CP analysis increasingly underestimates the number of steps above $N_{st} \sim 10$. One limitation for the MAP analysis is that the brightness of a single emitter is required as a prior and that variation due to the local molecular or cellular context can skew the results. However, efficient Markov chain Monte Carlo approaches should be able to characterize a rough likelihood for individual PSC traces without calibration and even avoid bias due to small photon budgets.

qSMLM

There now exist a number of visible light-based microscopy techniques capable of resolving nanometer-scale cellular features. Here, we limit our discussion to a category of these techniques collectively known as SMLM, which includes (direct) stochastic optical reconstruction microscopy ((d)STORM) (31–33), (fluorescence) photoactivation localization microscopy ((f)PALM) (34,35), and DNA point accumulation in nanoscale topography (DNA PAINT) (36,37), among others. SMLM relies upon harnessing sparse and random blinking of fluorescent labels to spatially dilute a fluorescent signal in time. The spatial coordinates of individual labeled molecules can then be determined or "localized" to a precision that scales like $\sigma/\sqrt{N_p}$, where σ is the width of the point-spread function and N_p is the number of collected photons. From the assembled table of localizations, a detailed image can be constructed with a spatial resolution well below the diffraction limit. Typically, SMLM can attain a 10–20 nm lateral resolution with slightly poorer depth resolution, although newer modalities like MINFLUX (38,39), ROSE (40), or SIMPLE (41), which combine SMLM with structured illumination, have shrunk the lateral resolution to $\sim$1 nm.

Beyond generating images, the datasets acquired by SMLM contain the necessary information for counting single molecules (42–45). If interpreted correctly, these datasets would reveal quantitative properties of cellular proteins such as their local concentration and oligomeric size. Because of the significantly increased spatial resolution, qSMLM could infer these properties for proteins expressed at relatively high densities or for complexes within close (10–50 nm) spatial proximity to one another (Fig. 3 *A*). In contrast, PSC often requires artificially modulating protein expression levels to reduce the density of protein complexes in the cell membrane. This is so that individual complexes may be resolved but may result in deviations from physiological activity of the protein under study (22,24).

While each localization identifies a single fluorophore, a single fluorescence emission period may span several frames, and, during the course of an experiment, one fluorophore may cycle multiple times between ON and OFF states (i.e., states that are visible or not visible, respectively, within the detection channel). Temporally consecutive localizations can, in theory, be clustered into a series of blinks emanating from each fluorophore. Blinking can lead to an over-estimation of the number of molecules if left unaccounted for, while any missed blinks arising from temporal binning, spatial overlap, background noise obscuring the signal, etc., can lead to an under-estimation in the count (46–48). This over- and under-counting can result in image artifacts, such as the apparent clustering of spatially uncorrelated molecules or degraded image reconstructions (49,50), and is particularly vexing for molecular counting applications.

Statistical spatial metrics such as pair-correlation analysis can differentiate the apparent clustering caused by multiple localizations of a single molecule from actual oligomers. The pair-correlation function provides a relative measure for the probability of detecting a molecule some distance r away from another when compared with that of a random distribution of molecules (Fig. 3 *Bi*). This metric enables the quantification of the density and radius of clusters as well as an estimate of the average number of monomers within a cluster (51,52). Recent extensions of this method are additionally able to provide image reconstructions with minimal blinking artifacts (53).

Over-counting can also be mitigated by temporally grouping blinks using prior knowledge of the photophysics

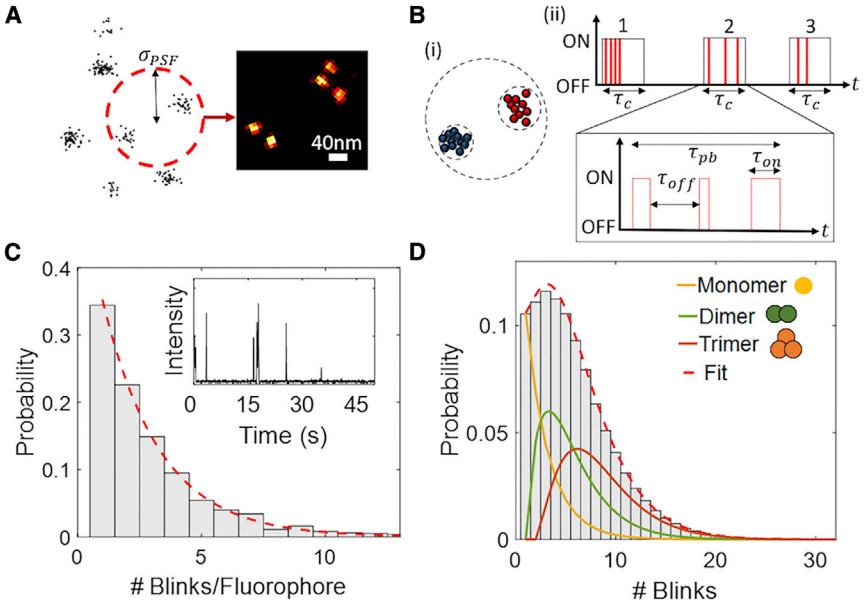

FIGURE 3 Quantitative single-molecule localization microscopy. (*A*) Pointillistic map of SMLM. The dashed (*red*) circle represents a point-spread function of radius σ_{PSF}. Given a typical SMLM resolution of 20 nm, the two molecules in the diffraction-limited spot can be visually differentiated. In rare cases, the subunits of a complex can be resolved (in this case, as a dimer and trimer). (*B*) More often, a spatial (i) or temporal (ii) analysis is employed to identify the composition of oligomeric complexes. The temporal analysis may involve determining photokinetic parameters such as ON times (τ_{ON}), OFF times (τ_{OFF}), and photobleaching times (τ_{PB}) to optimize a temporal bunching radius τ_C for clustering blinks. (*C*) The number of blinks emitted by many fluorophores used in SMLM follows a discrete exponential (geometric) distribution (simulated data). (*D*) The relative populations of oligomeric mixtures can be estimated from the blinking distribution of the ensemble (simulated data). To see this figure in color, go online.

of individual fluorophores. Calibrating for the characteristic dark time (τ_{off}) enables one to optimize a temporal threshold (τ_c) for associating blinks to a single molecule (Fig. 3 *B*ii) (49,54). The counting accuracy can be further improved by combining temporal clustering with pair-correlation or other spatial clustering methods (55–58). Characterizing the photokinetics of a fluorophore, however, can be challenging within the complex cellular environment but may be addressed by employing stochastic models of blinking such as hidden (59) or aggregated Markov models (60).

An alternative to spatially or temporally clustering localizations is to make use of the empirical observation that many fluorophores tend to blink a geometrically distributed number of times before photobleaching (54,61–63) (Fig. 3 *C*). Milstein et al. has shown that this information can be embedded into a statistical model that enables one to extract a maximum-likelihood estimate of the number of molecules from the observed number of blinks (64,65). Initially, a separate calibration was required to characterize the single fluorophore blink distribution. However, we have since shown that it is possible to apply an expectation-maximization-based learning algorithm to characterize the underlying blink distribution while simultaneously performing stoichiometric measurements in cells (Fig. 3 *D*), rendering the technique calibration free (66).

We recently explored the dynamic range of qSMLM in (67). Given that the duty cycle can be thought of as the probability of a fluorophore being ON in a given frame, a general rule of thumb is that the duty cycle must be much smaller than the inverse of the fluorophore density: duty cycle $<<$ 1/N, where N is the number of fluorophores within a diffraction limited volume (68). This translates to a dynamic range $\sim$100s of molecules for many imaging applications. However, this estimate does not account for effects due to the discretization of emissions into frames or photobleaching of fluorophores. In (67), we showed that the inverse scaling of the duty cycle with fluorophore density holds for both localizations and blinks when accounting for these experimental complexities and that accurate counting of $\sim$100s of molecules should still be attainable.

TECHNICAL REQUIREMENTS FOR SINGLE-MOLECULE COUNTING

There are several excellent review and methods articles that go into depth on the technical requirements of single-molecule imaging and counting (69–72). For a more complete perspective, we refer the reader to those resources and instead discuss here the technical issues either unique or particularly critical to molecular counting with PSC and qSMLM.

Bright and photostable fluorophores

Fluorescence stems from radiative relaxation from the first excited singlet state to the ground state on a nanosecond timescale. Intersystem crossing from the excited singlet to long-lived triplet states competes with fluorescence, resulting in intervals of low/dark signals (blinks). Single-fluorophore intensity traces with minimal blinking are desired for PSC applications, which requires decreasing the intersystem crossing rate and/or increasing the rate of triplet relaxation back to the ground state. Although photobleaching is a poorly understood process, two factors are important: excessive irradiation intensity and interaction with molecular oxygen via the triplet state (73). Long exposure

times, seconds to minutes, at relatively high excitation intensities (~10s–100s of W/cm^2) are needed to obtain high-quality PSC data that display well-defined stepwise drops in single-particle intensity traces (74). Therefore, it is imperative that experimental conditions are tuned to stabilize the emission of the fluorophore at a level well above the background noise while avoiding frequent blinking and premature photobleaching.

To meet such requirements, bright and photostable fluorophores are adopted for PSC experiments (Table 1). Molecular brightness, which is defined by the product of molar extinction coefficient ε (photon absorption ability) and fluorescence quantum yield φ_E (photon emission ability), determines the emission rate (photons/s) at a given excitation intensity. As shown in Table 1, photon budgets tend to vary by roughly an order of magnitude due to imaging conditions and estimation methods. Together with photostability (i.e., the average time to photobleaching), this determines the total photon budget per fluorophore N_{ph}. Typically, due to geometrical, optical, and detection limitations, less than 10% of the photon emission budget is recorded experimentally.

Fluorescent proteins (FPs), which are routinely co-expressed with proteins of interest, were first isolated and used for *in vivo* fluorescence imaging in the mid-1990s (87,88). Subsequently, a large collection of FPs with different excitation and emission spectra were developed and applied to fluorescence imaging studies across a range of biological systems (89). However, most FPs are not optimally suited for single-molecule observations. Apart from having relatively poor brightness and photostability, many popular FPs, including GFP and dsRED, can form homo-oligomers (90) and lead to an overestimation of the oligomer size via PSC or qSMLM analysis. Highly monomeric FPs, most of which have been engineered in direct response to this issue (91), should always be employed for counting. Still, incomplete maturation, common to all FPs to varying degrees, leads to sub-stoichiometric labeling and can cause an under-estimation of oligomer size (92,93). As such, careful control experiments on standard samples are needed to validate the results when using FP tags (26).

More recently, organic dyes (e.g., from the Alexa and Cy(anine) family) have been widely applied for PSC, benefiting from their smaller size, higher brightness, longer photostability, and more robust labeling chemistry (94). These dyes are attached to a target protein through either direct labeling (e.g., the fluorophore conjugated to a maleimide group interacts with a thiol group on a cysteine (95)) or indirect labeling (e.g., a dye-labeled synthetic peptide is attached through ligation (96,97)). While labeling efficiencies >90% can often be attained, the presence of unlabeled protein still causes an underestimation of the oligomer size, which needs to be accounted for in the data analysis. Moreover, these labeling strategies are widely used in purified samples and are not compatible with measurements in live cells. Conversely, rapid labeling via click chemistry (98) or protein tags for organic fluorophores, such as HaloTag (99), SNAP-tag (100), and CLIP-tag (101), enable fluorophore self-labeling of proteins in live cells. More recently, bright photostable dyes from Janelia Farms (e.g., JF646) and self-healing cyanine dyes that have a triplet quencher covalently attached (e.g., Lumidyne655) can extend observation times of labeled proteins to several minutes and significantly improve the accuracy and dynamic range of PSC estimates of molecular stoichiometry.

In addition to selecting the brightest and most photostable fluorophores, adequate photo-protectant imaging buffers are needed to optimize their photophysics. For PSC experiments, excursions to the triplet state should be minimized to ensure that an intensity drop corresponds to a photobleaching event and that the average step intensity is not lowered by fast averaging of ON and OFF emission states. To that end, quencher molecules are included in the imaging buffer to deactivate the triplet state back to the ground state

TABLE 1 Photophysical properties of fluorophores used in PSC

Fluorophore	$\lambda_{exc}/\lambda_{em}$ (nm)	ε ($\times 10^4$) ($M^{-1}cm^{-1}$)	φ_E	N_{ph} ($\times 10^3$)	TSQ	OXS	Refs
Alexa488	494/519	7.3	0.92	N/A	10 mM cysteamine, 50 mM Trp, 50 mM Met[a]	PCA/PCD[d]	(75,76)
EGFP	446/507	5.59	0.6	400	143 mM BME[b]	N/A	(33,77–79)
Cy3	554/568	15	0.04	270–3,000	0.4 mM Ni^{2+},1 mM COT, 2 mM NBA, 2 mM Trolox[c]	PCA/PCD	(19,72,75,77)
mCherry	587/610	7.2	0.22	150	5 mM Trolox	N/A	(78,80,81)
Cy5	646/662	25	0.27	50–650	0.4 mM Ni^{2+},143 mM BME, 1 mM COT, 2 mM NBA, 2 mM Trolox	GODCAT[e]	(19,72,75,77,82,83)
Alexa647	651/672	27	0.33	50–680	0.4 mM Ni^{2+},143 mM BME, 2 mM Trolox	GODCAT	(19,84–86)

The extinction coefficient (ε), quantum yield (φ_E), and the average photon budget (N_{ph}) all depend on the triplet state quenchers (TSQ) and oxygen scavengers (OXS) being used.
[a]TRP, tryptophan; MET, methionine.
[b]BME, β-mercaptoethanol.
[c]COT, cyclooctatetraene; NBA, 4-nitrobenzyl alcohol.
[d]PCA/PCD, 2.5 mM protocatechuic acid (PCA), 50 nM protocatechuate-3,3-dioxygenase (PCD).
[e]GODCAT, 100 nM glucose oxidase, 1.5 μM catalase, 56 mM glucose.

through a redox reaction (73). Table 1 lists the triplet quenchers (e.g., cysteamine, BME, Trolox) commonly used with the most popular fluorophores employed in PSC studies. Without adding a triplet quencher to the imaging buffer, the dissolved molecular oxygen quenches the fluorophore triplet state. The resulting reactive (singlet) oxygen chemically alters the fluorophore and causes a significant decrease in the time to photobleaching. Thus, oxygen scavenger compounds must be also included in the imaging buffer to extend the observation time and acquire PSC steps that are well separated in time. One of the first solutions implemented was the glucose-catalase (GODCAT) oxygen scavenger system (102), while later, the protocatechuic acid/protocatechuate-3,4-dioxygenase (PCA/PCD) system, which maintains pH, was adopted with good results (75). The two systems, triplet quencher and oxygen scavenger, may function differently for different fluorophores, and options used for popular fluorophores in PSC studies are listed in Table 1.

qSMLM similarly requires bright fluorophores (since the localization precision scales with the square root of the number of photons detected) and a quenched triplet state (leading to a photostable emission) (see Table 2). In contrast to PSC, qSMLM utilizes fluorophores that exhibit a sparse, intermittent emission pattern (i.e., blink). This is commonly achieved by utilizing photoswitchable (cycle between ON and dark state), photoactivatable (activate to ON), or photoconvertible (cycle between ON and a shifted frequency) fluorophores. Alternatively, blinking may also be achieved by controlling the binding/unbinding rate of a more conventional fluorophore to a target as in PAINT. Because of the various methods for obtaining a sparse emission, qSMLM requires excitation intensities ranging from $\sim$10s of W/cm^2 via PALM/PAINT up to several kW/cm^2 for dSTORM.

A range of organic fluorophores can be used for qSMLM (108), with Alexa 647 being by far the most common due to its superior brightness and photoconversion efficiency. For most organic dyes, efficient photoswitching requires an imaging buffer that contains both an enzymatic oxygen scavenging system and a primary thiol, often either β-mercaptoethanol or mercaptoethylamine. A number of promising dyes have recently been developed at Janelia Farms that are compatible with SMLM and can be induced to blink in standard dSTORM buffers (JF549/JF646) or can be photoactivated (PA-JF549) for PALM imaging (109). More recently, deuterated analogs of these dyes were synthesized that were found to be even brighter and more photostable (110). Likewise, improved imaging buffers (111,112), new self-healing dyes that obviate the need for additional photostabilizers (113–115), and spontaneously blinking dyes (116) typically increase the signal-to-noise ratio while reducing the environmental sensitivity of the fluorophores.

When performing qSMLM with organic fluorophores, the labels must still be introduced into the cell and attached to a target protein with high efficiency and specificity. Perhaps the most common approach is through immunolabeling, but this can result in clustering artifacts due to the large size of the antibodies and multiply bound, fluorescently labeled secondary antibodies. An alternative is to employ cell-permeable protein tags used for PSC and other SMF imaging applications in live cells (e.g., SNAP-tag or HaloTag), which have also become increasingly popular for super-resolved imaging (117). Again, these methods can achieve a labeling efficiency >90%, making them ideal for qSMLM.

Alternatively, photoactivatable/convertible FPs (e.g., Dendra2, mMaple, and PA-mCherry) may be employed for qSMLM, with the primary advantage being that they can be genetically expressed with a protein of interest to maintain a desired one-to-one labeling. At present, however, the labeling efficiency of FPs is limited to $\sim$70% due to incomplete maturation and inefficient photoactivation/conversion (92,93). If the maturation rate and photoactivation/conversion efficiency are known, these factors can be corrected for using appropriate mathematical models (92); however, in general, such low labeling efficiency is problematic. Likewise, as mentioned above, FPs also tend to dimerize or form higher-order oligomers (90), particularly at high concentrations, and typically emit 1–2 orders of magnitude less photons than some of the best organic dyes (108). With that said, in recent years, bright and

TABLE 2 Photophysical properties of common fluorophores used in qSMLM

Fluorophore	$\lambda_{exc}/\lambda_{em}$ (nm)	λ_{act} (nm)	ε ($\times 10^4$) ($M^{-1}cm^{-1}$)	φ_E	DC ($\times 10^{-4}$)	N_{blinks}	N_{ph} ($\times 10^3$)	Refs
mEOS3.2	516/580	405	6.34	0.84	0.03	2.4	1.2–2.8	(103–105)
mMaple3	566/583	405	3.0	0.74	0.006	2.8	1.8–2.6	(105,106)
PAmCherry1	564/595	405	1.8	0.46	0.08	1.0	0.7	(104,107)
Dendra2	561/573	405	4.5	0.5	0.04	2.7	0.4–1.8	(104,105)
Atto488	501/523	N/A	9.0	0.8	6–22	11–49	3–4	(105,108)
Atto565	563/593	N/A	12.0	0.9	3.7–5.8	4–5	60–89	(108)
Cy5	648/670	N/A	25.0	0.28	4–7	10–17	57–79	(108)
Alexa647	650/665	N/A	23.9	0.33	1.3–12	3–28	85–117	(105,108)

The extinction coefficient (ε), quantum yield (φ_E), duty cycle (DC), average number of blinks (N_{blinks}), and the average photon budget (N_{ph}) all depend on the chemical environment of the fluorophore and therefore vary depending on the imaging conditions. A common characteristic is that fluorescent proteins can reach much lower duty cycles than many organic fluorophores but typically undergo fewer blinking cycles and emit less photons.

monomeric FPs, such as mEos3.2 and PA-mKate2, have been developed for SMLM applications (103,104).

SMF counting instrumentation or step counting requires more than a FitBit

The most common instrument used for single-molecule counting is the total internal reflection fluorescence (TIRF) microscope (118), which employs excitation via the evanescent field at an interface between a glass coverslip and the sample solution. The penetration depth of the exponentially decaying evanescent wave is ~100 nm for visible light, resulting in excitation of labeled particles that are confined transiently or permanently at the interface and ensuring a superior signal-to-noise ratio compared with confocal microscopes. With this advantage, the photobleaching steps or blinks of fluorophores can be counted more unambiguously without interference from the background signal. TIRF is commonly achieved using an objective with a high numerical aperture (>1.45) to ensure that the incident angle of the excitation beam at the glass/water interface is larger than the critical angle, as is shown in Fig. 1 *A*. The red-shifted emission is separated from the back-reflected excitation via appropriate dichroic mirrors and long- and band-pass filters.

While the instrumentation needed for SMF counting is similar to that used for general TIRF imaging, recent improvements in detector technology and illumination shaping techniques have enhanced the accuracy of PSC and qSMLM data analysis. In the early days of SMF imaging via TIRF, the most widely used camera was the charge-coupled device (CCD) and, later, the improved electron-multiplying CCD (EMCCD). EMCCD technology has been dominant for many years for single-molecule imaging applications due to its high quantum efficiency (~90%) and on-chip amplification, which renders it virtually single-photon sensitive (119,120). Although EMCCDs are still unmatched at overcoming readout noise in the low-signal regime (<10 photons/pixel), in recent years, scientific complimentary metal-oxide semiconductor (sCMOS) cameras have begun to replace EMCCD cameras in SMLM applications. While CMOS cameras have long offered higher frames rates and larger fields of view at a lower cost than CCD-based detectors, their previously limited quantum efficiency (~60%) and pixel-dependent noise properties hindered their use in SMF imaging (121,122). As the quantum efficiency of sCMOS cameras is now comparable to that of EMCCD cameras (122), they can now match or even outperform EMCCD cameras in many SMLM applications (123).

For most SMF imaging applications, illumination is with the typical Gaussian-shaped profile of commercial lasers. For both imaging and counting applications, this inhomogeneous illumination limits the field of view that can be recorded, as the rate of fluorophore excitation and emission changes as a function of position. In addition, for counting techniques that require a calibration, a non-uniform illumination profile may affect the fluorophore photophysics. Typically, the excitation beam is expanded to make the illumination quasi-homogenous over the detection area, but this necessitates higher power and more expensive lasers and will prebleach a larger area of the sample outside the field of view. To overcome these challenges, several groups have developed methods to flatten the illumination profile into a so-called top-hat profile. These methods involve inserting an optical element in the laser path such as specialized optical fiber setups (124,125), beam shapers (126,127), or rapid scanning using shakeable mirrors (128). Many of the proposed methods to achieve flat-top illumination profiles are also compatible with a TIRF illumination geometry. Flat-top illumination also allows the extension of the usable field of view to make complete use of the larger detector areas of sCMOS cameras (129).

Calibration standards and control experiments

Any molecular counting measurement requires a proper set of experimental controls. In (26), we used surface immobilized EGFP concatemers of up to four identical units to calibrate the PSC analysis of purified muscarinic M_2 receptor and an afferent G_i protein. As proof of principle for the Bayesian MAP method (30), we used self-assembled interleaving DNA structures ("ladders") formed by partially complementary DNA strands, each labeled with a Cy5 dye. Similarly, several *in vitro* surface assays to characterize the photophysical properties of fluorophores for qSMLM have been proposed. Golfetto et al. (130) developed surface assay for molecular isolation (SAMI) from fluorescent ligands that bind to a specific target site on engineered antibody fragments. Nucleic-acid-based platforms created from two- and three-dimensional DNA origami structures have been developed as calibration both for dSTORM (131,132) and, adapted from a commercial template, for qPAINT (133). The reader is referred to the excellent protocol for designing and building standardized DNA origami structures by Schmied et al. (134). Note that DNA origami structures, with appropriate labels and buffer conditions, can also be used as standards in PSC studies.

A serious concern with any *in vitro* calibration is that the cellular environment may alter the fluorophore photophysics. The most straightforward solution would be to perform calibration measurements on intracellular proteins with well-known stoichiometries. In (65), we used monomeric variants of the carcinoembryonic antigen-related cellular adhesion molecules to calibrate for the blinking distribution of Alexa647 for qSMLM. Similarly, monomeric cell surface receptors CD86 with either one or two SNAP tags fused to their N-terminus were used as effective controls for in-cell studies of GPCR oligomerization (135).

Several groups have proposed more general intracellular protein-based standards for molecular counting. In *Xenopus*

oocytes, the human glycine receptor has a well-defined, stable stoichiometry of either two, three, or five, dependent upon which subunit is labeled and expressed. This feature was directly used to calibrate for the photoconversion/activation efficiency of many commonly employed, photoconvertible/activatable FPs including mEOS3.1, Dendra2, mMaple, and PA-mCherry (136). Similarly, homo-oligomeric bacterial proteins such as FsaA, GlnA, and FtnA, with respective stoichiometries of 10, 12, and 24, can be employed in a similar fashion and can be expressed and assembled in mammalian cells (137). The nuclear pore complex (NPC) appears to be a particularly versatile calibration standard both for imaging and counting (92). A variety of nucleoporins (Nups), which make up much of the structure of the NPC, are present at a conserved copy number and can be co-expressed with either an appropriate FP or a SNAP-tag/HaloTag for covalent labeling by an organic dye. For instance, in (92), Nup 96 (present at 32 copies per NPC) was employed as a standard within human embryonic kidney cells to quantify the abundance of several other Nups. Nup 188 (at 16 copies per NPC) was similarly used as a calibration standard within *Saccharomyces cerevisiae*.

APPLICATIONS TO GPCR OLIGOMERIZATION

Supramolecular architectures of proteins are intimately related to their cooperative and regulatory behavior, with hemoglobin as a classic example. It is therefore tempting to speculate that oligomers of GPCRs are conducive to inter-protomer interactions that give rise to signaling cooperativity and the complex ligand-binding effects observed experimentally, which cannot be explained by the classic ternary model (138). Single-molecule counting methods can quantify the composition of ternary protein complexes, which can delineate the mechanistic pathway of activation and signaling involving oligomers of GPCRs coupled to oligomers of G proteins.

The oligomeric size of detergent-purified muscarinic M_2 receptor (M_2R) and of attendant G_{i1} protein was measured by PSC by Gradinaru et al. (26). The two proteins were tagged with EGFP and examined via TIRF imaging, both separately and coupled together in a co-purified M_2R-G_{i1} complex (Fig. 4). The photobleaching behavior was calibrated using concatemers of EGFP of known oligomeric size, purified to homogeneity. Immobilized particles of the purified EGFP-tagged M_2R displayed up to six photobleaching steps. The distribution of intensities from only four of those steps resembled the distribution from single fluorophores in multiplexed controls, suggesting that M_2R was purified primarily as a tetramer. The oligomeric state of the receptor was essentially unaffected by ligand binding. In contrast, EGFP-tagged G_{i1} was purified primarily as hexamers, and G-protein oligomerization appeared to be stabilized through interactions between the α-subunits. Interestingly, coupling of M_2R and G_{i1} resulted in a supramolecular complex of four receptors and four G proteins (Fig. 4 *C* and *E*). In this octameric complex, simultaneous activation of the receptor by agonist and of the G protein by GTP led to a reduction in the oligomeric size of the latter to monomers and dimers (Fig. 4 *F*). These *in vitro* findings were supported by a follow-up study in live cells (139), where we reported significant levels of oligomeric M_2R and G_{i1} using fluorescence cross-correlation spectroscopy. We discovered that agonist ligands promote transient coupling of otherwise independent oligomers of the two proteins.

Lohse et al. (135) exploited TIRF single-particle tracking in live cells to determine the oligomeric sizes of β_1-adrenergic receptor, the β_2-adrenergic receptor, and the $GABA_B$ receptor. Receptors were labeled with Alexa647 via an extracellular N-terminal SNAP-tag, and monomeric and dimeric controls (CD86 with one or two SNAP tags) were used for validation and correction for random colocalization. By integrating PSC analysis with Gaussian fitting of trace intensities, the authors found that the β_1-adrenergic receptor was ∼80% monomeric and showed an increasing fraction of dimers at higher expression levels, while the β_2-adrenergic receptor was predominantly dimeric (∼60%) at low densities (∼0.1 particle/μm^2)

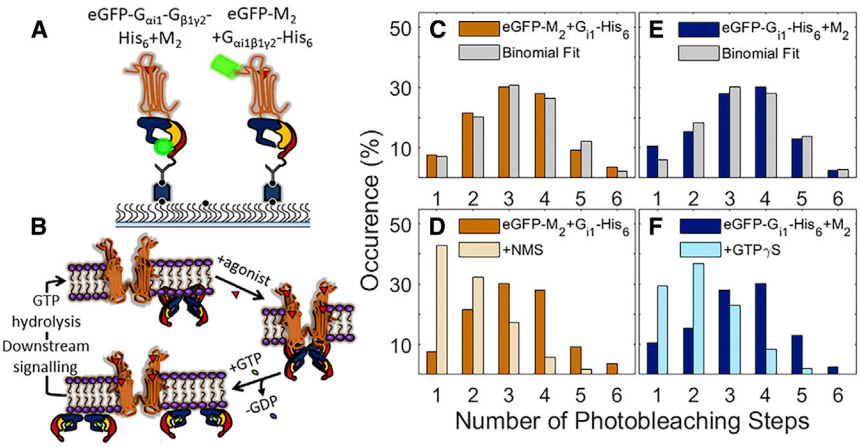

FIGURE 4 (*A*) Photobleaching of surface-tethered, receptor-coupled EGFP-Gi and G_{i1}-coupled EGFP-M_2 receptor. (*B*) The data support the existence of a stable hetero-octamer (four M_2 receptors coupled to four G_{i1} proteins) that, upon activation of both the receptor and the G protein, dissociates into smaller subunits. (*C* and *E*) The distribution of photobleaching steps for each complex was fit to a binomial distribution ($n = 6$, $p = 0.58$, $N_{avg} = np = 3.5$). Further filtering using monomeric controls of the step intensity distribution suggested that both M_2 receptor and G_{i1} are most probably tetrameric in complex with each other. (*D*) The number of steps decreased significantly for the labeled receptor in the presence of antagonist ligand, 10 μM NMS, (*F*) and for the labeled G protein in the presence of 10 μM GTPγS. Data are reproduced with permission from (26). To see this figure in color, go online.

and formed significant fractions of tri- and tetramers at higher densities (~0.5 particle/μm^2). In contrast, the γ-aminobutyric acid receptor, a prototypical family-C GPCR, consisted prevalently of heterodimers at low densities and of tetramers (dimers of dimers) and octamers (tetramers of dimers) at high densities. A similar approach from the same authors has recently revealed that the chemokine receptor CXR4, which is a primary target for drug development, exhibits transient oligomerization that is disrupted by inverse agonists binding to a minor sub-pocket of the receptor (140).

Other family-C receptors, such as metabotropic glutamate (mGlu) and calcium-sensing receptors have been shown to form functional dimers using single-molecule methods.

Vafabakhsh et al. used subunit counting to investigate homodimerization and heterodimerization of purified mGluRs tagged with GFP (141). They found evidence that mGluR2 forms homodimers mediated by interactions between ligand-binding domains. Using two-color PSC on GFP- and mCherry-tagged receptors, they also showed that mGluR2 readily forms heterodimers with other subtypes of mGluRs, especially mGluR3. By combining PSC and single-molecule fluorescence resonance energy transfer data, the authors proposed a model of cooperativity gating within mGluR heterodimers that produces both basal activity and a non-linear response and may be adapted to respond to distinct spatiotemporal synaptic glutamate profiles.

One of the earliest efforts to apply qSMLM to the study of GPCRs was reported in Jonas et al. (142). Employing dual-color PALM with photoactivatable dyes, Jonas et al. probed the high degree of oligomerization of two functionally defined mutants of the luteinizing hormone receptor (LHR): LHRB− and LHRS−. The high spatial resolution they were able to attain (~8 nm) enabled them to directly resolve individual receptors in distinct oligomeric complexes. In fact, they were able to infer the existence of complexes ranging from trimers to oligomers containing as many as 9 protomeric receptors. The ratio of LHRB− to LHRS− in complex modulates the ligand-induced signal sensitivity. Quantitative PALM imaging of these oligomeric complexes was able to reveal both their abundance as well as details on the structural organization of the individual protomers within the various oligomers.

More recently, quantitative dSTORM was used to investigate the nanoscale organization of the mGluR4 at presynaptic active zones in the mouse cerebellum (143). Multiple nanodomains were imaged inside active zones, each containing either monomers or dimers of mGluR4. The study provided direct support for the existence of endogenous mGluR4 dimers and implicated mGluR4 in regulating voltage-gated calcium channels and/or the secretory mechanisms involved in synaptic transmission. Similarly, Möller et al. (144) applied quantitative dSTORM imaging to assess the monomer-dimer equilibrium of SNAP-tag labeled μ-opioid receptors, a pharmaceutical target for chronic pain. They found that while the wild-type receptors were strictly monomeric, ~80% of receptors in the constitutively active mutant T279K existed as dimers. Likewise, upon stimulation by a full agonist (DAMGO), ~90% of the μ-opioid receptors were detected as dimers. Their analysis was supported by employing the β1-adrenergic receptor as a monomeric control and CD28 as a dimeric control.

An alternative approach employing qPAINT, which may overcome some of the over-counting artifacts that plague dSTORM and PALM, has very recently been adapted to study the oligomerization of the purinergic receptor Y2 (P2Y2) (145). P2Y2 is a rhodopsin-like GPCR expressed at high levels and was studied within a pancreatic cancer cell line. It was revealed that while the density of P2Y2 receptors was unchanged in the presence of an antagonist, a reduced number of receptors were concomitantly found as oligomers. Conversely, treatment by an agonist did not affect the oligomeric state of the receptors.

Finally, advances in fluorophore technology, developed expressly for qSMLM, are set to accelerate our understanding of GPCRs. For instance, self-blinking carbon dots (CDs) are both relatively insensitive to the local environment and can be tuned to yield a single, bright burst of fluorescence. He et al. (146) employed antibody fragment-conjugated CDs to study the chemokine receptor CXCR4, which is a potential drug target for HIV and several cancer types. Because the CDs each emitted only a single blink, He et al. could simply cluster and count the localizations to ascertain the extent of oligomerization within each cluster. These novel fluorophores enabled them to report both the endogenous dimerization of CXCR4 and to map the spatial distribution of the ligand-regulated receptors on the cell membrane.

The studies described above challenge the notion of monomers as the exclusive element of signaling while raising important questions about the nature and role of GPCR oligomers. A significant involvement of oligomers in GPCR-mediated signaling has implications for understanding the underlying mechanism and its role in disease, and it opens up exciting new approaches to therapeutic intervention. Furthermore, supramolecular oligomeric receptor-G protein complexes, transient or (meta)stable, offer a viable mechanism for multiple signaling pathways and biased agonism (15,147).

SUMMARY AND OUTLOOK

SMF counting techniques have matured considerably in recent years due to advances in fluorophore photophysics, imaging technology, and data analysis. Table 3 highlights the most salient advantages (pros) and disadvantages (cons) of molecular counting with both PSC and qSMLM. The methodology described here is ready to be deployed for a wealth of applications aimed at disentangling the size, organization, and dynamics of supramolecular complexes. We focused on recent studies that revealed the oligomerization state of several GPCRs and the role of these oligomers in signaling. Oligomers of G proteins have received much less attention, and they have typically been

TABLE 3 Advantages and disadvantages of PSC and qSMLM

Technique	Pros	Cons
PSC	• directly identifies the oligomeric state of individual molecular complexes • provides super-resolved structural information about individual oligomers • can be employed in live cells/on dynamic complexes	• ability to identify individual oligomers is diffraction limited; may need to artificially reduce protein density/expression levels • challenging to count large oligomeric complexes (>8-10 protomers)
qSMLM	• allows counting at high densities/protein expression • possible to quantify large complexes (∼100s of protomers) • provides structural information about individual oligomers • complemented by super-resolved spatial imaging	• limited to fixed samples or slowly moving target proteins • sensitive to cellular environment/requires careful calibration • typically does not identify individual oligomers, rather, provides information on oligomeric fractions within a cell

discarded as artifacts of purification; however, future single-molecule studies in live cells should reveal their diffusion and oligomerization dynamics and document their involvement in the signaling process. Furthermore, counting experiments coupled with molecular dynamics simulations and site-directed mutagenesis can provide a map of critical inter-monomer contacts with receptor and/or G protein oligomers. The results will be vital for defining the energetics and the architecture of oligomeric assemblies of GPCRs and will provide useful insights for the development of novel drugs that control oligomer formation.

AUTHOR CONTRIBUTIONS

All authors contributed to writing the manuscript. D.F.N. and X. Z. assembled the tables and figures. X. Z. and D. F. N. collected the data in Figs. 2 and 3, respectively.

ACKNOWLEDGMENTS

This work was supported by Discovery Grants from the Natural Sciences and Engineering Research Council of Canada (RGPIN 2017–06030 to C.C.G. and RGPIN 418251 for J.N.M.). The authors thank Horacio Septien Gonzalez and Dr. Dennis Fernandes for assisting with figures in the manuscript.

DECLARATION OF INTERESTS

The authors declare no competing interests.

REFERENCES

1. Ishikawa, K. 2021. Multilayered regulation of proteome stoichiometry. *Curr. Genet.* 67:883–890.
2. Marsh, J. A., and S. A. Teichmann. 2015. Structure, dynamics, assembly, and evolution of protein complexes. *Annu. Rev. Biochem.* 84:551–575.
3. Clark, N. M., A. P. Fisher, …, R. Sozzani. 2020. Protein complex stoichiometry and expression dynamics of transcription factors modulate stem cell division. *Proc. Natl. Acad. Sci. USA.* 117:15332–15342.
4. Brandenberg, O. F., C. Magnus, …, A. Trkola. 2017. Predicting HIV-1 transmission and antibody neutralization efficacy in vivo from stoichiometric parameters. *PLoS Pathog.* 13:e1006313.
5. Fredriksson, R., M. C. Lagerström, …, H. B. Schiöth. 2003. The G-protein-coupled receptors in the human genome form five main families. Phylogenetic analysis, paralogon groups, and fingerprints. *Mol. Pharmacol.* 63:1256–1272.
6. Katritch, V., V. Cherezov, and R. C. Stevens. 2012. Diversity and modularity of G protein-coupled receptor structures. *Trends Pharmacol. Sci.* 33:17–27.
7. Sriram, K., and P. A. Insel. 2018. GPCRs as targets for approved drugs: how many targets and how many drugs? *Mol. Pharmacol.* https://doi.org/10.1124/mol.117.111062.
8. Juette, M. F., D. S. Terry, …, S. C. Blanchard. 2016. Single-molecule imaging of non-equilibrium molecular ensembles on the millisecond timescale. *Nat. Methods.* 13:341–344.
9. Tian, H., A. Fürstenberg, and T. Huber. 2017. Labeling and single-molecule methods to monitor G protein-coupled receptor dynamics. *Chem. Rev.* 117:186–245.
10. Felce, J. H., S. L. Latty, …, S. J. Davis. 2017. Receptor quaternary organization explains G protein-coupled receptor family structure. *Cell Rep.* 20:2654–2665.
11. Rosenbaum, D. M., S. G. F. Rasmussen, and B. K. Kobilka. 2009. The structure and function of G-protein-coupled receptors. *Nature.* 459:356–363.
12. Manglik, A., and A. C. Kruse. 2017. Structural basis for G protein-coupled receptor activation. *Biochemistry.* 56:5628–5634.
13. Ferré, S., V. Casadó, …, X. Guitart. 2014. G protein–coupled receptor oligomerization revisited: functional and pharmacological perspectives. *Pharmacol. Rev.* 66:413–434.
14. Milligan, G., R. J. Ward, and S. Marsango. 2019. GPCR homo-oligomerization. *Curr. Opin. Cell Biol.* 57:40–47.

15. Sleno, R., and T. E. Hébert. 2019. Shaky ground - the nature of metastable GPCR signalling complexes. *Neuropharmacology.* 152:4–14.
16. von Diezmann, L., Y. Shechtman, and W. E. Moerner. 2017. Three-dimensional localization of single molecules for super-resolution imaging and single-particle tracking. *Chem. Rev.* 117:7244–7275.
17. Feng, X. A., M. F. Poyton, and T. Ha. 2021. Multicolor single-molecule FRET for DNA and RNA processes. *Curr. Opin. Struct. Biol.* 70:26–33.
18. Ghosh, A., and J. Enderlein. 2021. Advanced fluorescence correlation spectroscopy for studying biomolecular conformation. *Curr. Opin. Struct. Biol.* 70:123–131.
19. Gong, W., P. Das, …, Z. Yang. 2019. Redefining the photo-stability of common fluorophores with triplet state quenchers: mechanistic insights and recent updates. *Chem. Commun.* 55:8695–8704.
20. Gordon, M. P., T. Ha, and P. R. Selvin. 2004. Single-molecule high-resolution imaging with photobleaching. *Proc. Natl. Acad. Sci. USA.* 101:6462–6465.
21. Engel, B. D., W. B. Ludington, and W. F. Marshall. 2009. Intraflagellar transport particle size scales inversely with flagellar length: revisiting the balance-point length control model. *J. Cell Biol.* 187:81–89.
22. Ulbrich, M. H., and E. Y. Isacoff. 2007. Subunit counting in membrane-bound proteins. *Nat. Methods.* 4:319–321.
23. Leake, M. C., J. H. Chandler, …, J. P. Armitage. 2006. Stoichiometry and turnover in single, functioning membrane protein complexes. *Nature.* 443:355–358.
24. Das, S. K., M. Darshi, …, H. Bayley. 2007. Membrane protein stoichiometry determined from the step-wise photobleaching of dye-labelled subunits. *Chembiochem.* 8:994–999.
25. Gallistel, C. R., S. Fairhurst, and P. Balsam. 2004. The learning curve: implications of a quantitative analysis. *Proc. Natl. Acad. Sci. USA.* 101:13124–13131.
26. Shivnaraine, R. V., D. D. Fernandes, …, C. C. Gradinaru. 2016. Single-molecule analysis of the supramolecular organization of the M2 muscarinic receptor and the Gαi1 protein. *J. Am. Chem. Soc.* 138:11583–11598.
27. Tsekouras, K., T. C. Custer, …, S. Pressé. 2016. A novel method to accurately locate and count large numbers of steps by photobleaching. *Mol. Biol. Cell.* 27:3601–3615.
28. Hummert, J., K. Yserentant, …, D.-P. Herten. 2021. Photobleaching step analysis for robust determination of protein complex stoichiometries. *Mol. Biol. Cell.* 32:ar35.
29. Li, H., and H. Yang. 2019. Statistical learning of discrete states in time series. *J. Phys. Chem. B.* 123:689–701.
30. Garry, J., Y. Li, …, A. D. Rutenberg. 2020. Bayesian counting of photobleaching steps with physical priors. *J. Chem. Phys.* 152:024110.
31. Heilemann, M., S. Van De Linde, …, M. Sauer. 2009. Super-resolution imaging with small organic fluorophores. *Angew. Chem. Int. Ed. Engl.* 48:6903–6908.
32. Heilemann, M., S. van de Linde, …, M. Sauer. 2008. Subdiffraction-resolution fluorescence imaging with conventional fluorescent probes. *Angew. Chem. Int. Ed. Engl.* 47:6172–6176.
33. Rust, M. J., M. Bates, and X. Zhuang. 2006. Sub-diffraction-limit imaging by stochastic optical reconstruction microscopy (STORM). *Nat. Methods.* 3:793–795.
34. Betzig, E., G. H. Patterson, …, H. F. Hess. 2006. Imaging intracellular fluorescent proteins at nanometer resolution. *Science.* 313:1642–1645.
35. Nan, X., E. A. Collisson, …, S. Chu. 2013. Single-molecule superresolution imaging allows quantitative analysis of RAF multimer formation and signaling. *Proc. Natl. Acad. Sci. USA.* 110:18519–18524.
36. Jungmann, R., C. Steinhauer, …, F. C. Simmel. 2010. Single-molecule kinetics and super-resolution microscopy by fluorescence imaging of transient binding on DNA origami. *Nano Lett.* 10:4756–4761.
37. Schnitzbauer, J., M. T. Strauss, …, R. Jungmann. 2017. Super-resolution microscopy with DNA-PAINT. *Nat. Protoc.* 12:1198–1228.
38. Balzarotti, F., Y. Eilers, …, S. W. Hell. 2017. Nanometer resolution imaging and tracking of fluorescent molecules with minimal photon fluxes. *Science.* 355:606–612.
39. Schmidt, R., T. Weihs, …, S. W. Hell. 2021. MINFLUX nanometer-scale 3D imaging and microsecond-range tracking on a common fluorescence microscope. *Nat. Commun.* 12:1478.
40. Gu, L., Y. Li, …, W. Ji. 2019. Molecular resolution imaging by repetitive optical selective exposure. *Nat. Methods.* 16:1114–1118.
41. Reymond, L., J. Ziegler, …, S. Wieser. 2019. SIMPLE: structured illumination based point localization estimator with enhanced precision. *Opt Express.* 27:24578–24590.
42. Shivanandan, A., H. Deschout, …, A. Radenovic. 2014. Challenges in quantitative single molecule localization microscopy. *FEBS Lett.* 588:3595–3602.
43. Baddeley, D., and J. Bewersdorf. 2018. Biological insight from super-resolution microscopy: what we can learn from localization-based images. *Annu. Rev. Biochem.* 87:965–989.
44. Jung, S.-R., B. S. Fujimoto, and D. T. Chiu. 2017. Quantitative microscopy based on single-molecule fluorescence. *Curr. Opin. Chem. Biol.* 39:64–73.
45. Jungmann, R., M. S. Avendaño, …, P. Yin. 2016. Quantitative super-resolution imaging with qPAINT. *Nat. Methods.* 13:439–442.
46. Annibale, P., S. Vanni, …, A. Radenovic. 2011. Quantitative photo activated localization microscopy: unraveling the effects of photoblinking. *PLoS One.* 6:e22678.
47. Deschout, H., A. Shivanandan, …, A. Radenovic. 2014. Progress in quantitative single-molecule localization microscopy. *Histochem. Cell Biol.* 142:5–17.
48. Durisic, N., L. L. Cuervo, and M. Lakadamyali. 2014. Quantitative super-resolution microscopy: pitfalls and strategies for image analysis. *Curr. Opin. Chem. Biol.* 20:22–28.
49. Annibale, P., S. Vanni, …, A. Radenovic. 2011. Identification of clustering artifacts in photoactivated localization microscopy. *Nat. Methods.* 8:527–528.
50. Rossboth, B., A. M. Arnold, …, G. J. Schütz. 2018. TCRs are randomly distributed on the plasma membrane of resting antigen-experienced T cells. *Nat. Immunol.* 19:821–827.
51. Sengupta, P., T. Jovanovic-Talisman, …, J. Lippincott-Schwartz. 2011. Probing protein heterogeneity in the plasma membrane using PALM and pair correlation analysis. *Nat. Methods.* 8:969–975.
52. Sengupta, P., T. Jovanovic-Talisman, and J. Lippincott-Schwartz. 2013. Quantifying spatial organization in point-localization superresolution images using pair correlation analysis. *Nat. Protoc.* 8:345–354.
53. Bohrer, C. H., X. Yang, …, J. Xiao. 2021. A pairwise distance distribution correction (DDC) algorithm to eliminate blinking-caused artifacts in SMLM. *Nat. Methods.* 18:669–677.
54. Lee, S.-H., J. Y. Shin, …, C. Bustamante. 2012. Counting single photoactivatable fluorescent molecules by photoactivated localization microscopy (PALM). *Proc. Natl. Acad. Sci. USA.* 109:17436–17441.
55. Puchner, E. M., J. M. Walter, …, W. A. Lim. 2013. Counting molecules in single organelles with superresolution microscopy allows tracking of the endosome maturation trajectory. *Proc. Natl. Acad. Sci. USA.* 110:16015–16020.
56. Coltharp, C., R. P. Kessler, and J. Xiao. 2012. Accurate construction of photoactivated localization microscopy (PALM) images for quantitative measurements. *PLoS One.* 7:e51725.
57. Lillemeier, B. F., M. A. Mörtelmaier, …, M. M. Davis. 2010. TCR and Lat are expressed on separate protein islands on T cell membranes and concatenate during activation. *Nat. Immunol.* 11:90–96.
58. Buss, J., C. Coltharp, …, J. Xiao. 2013. In vivo organization of the FtsZ-ring by ZapA and ZapB revealed by quantitative super-resolution microscopy. *Mol. Microbiol.* 89:1099–1120.
59. Patel, L., N. Gustafsson, …, E. Cohen. 2019. A hidden Markov model approach to characterizing the photo-switching behavior of fluorophores. *Ann. Appl. Stat.* 13:1397–1429.

60. Rollins, G. C., J. Y. Shin, …, S. Pressé. 2015. Stochastic approach to the molecular counting problem in superresolution microscopy. *Proc. Natl. Acad. Sci. USA.* 112:E110–E118.

61. Nieuwenhuizen, R. P. J., M. Bates, …, S. Stallinga. 2015. Quantitative localization microscopy: effects of photophysics and labeling stoichiometry. *PLoS One.* 10:e0127989.

62. Fricke, F., J. Beaudouin, …, M. Heilemann. 2015. One, two or three? Probing the stoichiometry of membrane proteins by single-molecule localization microscopy. *Sci. Rep.* 5:14072.

63. Wang, Y., P. Penkul, and J. N. Milstein. 2016. Quantitative localization microscopy reveals a novel organization of a high-copy number plasmid. *Biophys. J.* 111:467–479.

64. Nino, D., N. Rafiei, …, J. N. Milstein. 2017. Molecular counting with localization microscopy: a bayesian estimate based on fluorophore statistics. *Biophys. J.* 112:1777–1785.

65. Nino, D., D. Djayakarsana, and J. N. Milstein. 2019. Nanoscopic stoichiometry and single-molecule counting. *Small Methods.* 3:1900082.

66. Boonkird, A., D. F. Nino, and J. N. Milstein. 2021. An expectation-maximization approach to quantifying protein stoichiometry with single-molecule imaging. *Bioinformatics Adv.* 1. https://doi.org/10.1093/bioadv/vbab032.

67. Nino, D. F., and J. N. Milstein. 2021. Estimating the dynamic range of quantitative single-molecule localization microscopy. *Biophys. J.* 120:3901–3910.

68. van de Linde, S., S. Wolter, …, M. Sauer. 2010. The effect of photoswitching kinetics and labeling densities on super-resolution fluorescence imaging. *J. Biotechnol.* 149:260–266.

69. Zhang, H., and P. Guo. 2014. Single molecule photobleaching (SMPB) technology for counting of RNA, DNA, protein and other molecules in nanoparticles and biological complexes by TIRF instrumentation. *Methods.* 67:169–176.

70. Dey, S., and S. Maiti. 2018. Single-molecule photobleaching: instrumentation and applications. *J. Biosci.* 43:447–454.

71. Lelek, M., M. T. Gyparaki, …, C. Zimmer. 2021. Single-molecule localization microscopy. *Nat. Rev. Methods Primers.* 1:39–47.

72. Vangindertael, J., R. Camacho, …, K. P. F. Janssen. 2018. An introduction to optical super-resolution microscopy for the adventurous biologist. *Methods Appl. Fluoresc.* 6:022003.

73. Vogelsang, J., R. Kasper, …, P. Tinnefeld. 2008. A reducing and oxidizing system minimizes photobleaching and blinking of fluorescent dyes. *Angew. Chem. Int. Ed. Engl.* 47:5465–5469.

74. Deschenes, L. A., and D. A. Vanden Bout. 2002. Single molecule photobleaching: increasing photon yield and survival time through suppression of two-step photolysis. *Chem. Phys. Lett.* 365:387–395.

75. Aitken, C. E., R. A. Marshall, and J. D. Puglisi. 2008. An oxygen scavenging system for improvement of dye stability in single-molecule fluorescence experiments. *Biophys. J.* 94:1826–1835.

76. Chen, H., S. S. Ahsan, …, W. W. Webb. 2010. Mechanisms of quenching of Alexa fluorophores by natural amino acids. *J. Am. Chem. Soc.* 132:7244–7245.

77. Zhao, Q., I. T. Young, and J. G. S. de Jong. 2011. Photon budget analysis for fluorescence lifetime imaging microscopy. *J. Biomed. Opt.* 16:086007.

78. Wang, S., J. R. Moffitt, …, X. Zhuang. 2014. Characterization and development of photoactivatable fluorescent proteins for single-molecule–based superresolution imaging. *Proc. Natl. Acad. Sci. USA.* 111:8452–8457.

79. Krasowska, J., M. Olasek, …, B. Wielgus-Kutrowska. 2010. The comparison of aggregation and folding of enhanced green fluorescent protein (EGFP) by spectroscopic studies. *Spectroscopy.* 24:343–348.

80. Heppert, J. K., D. J. Dickinson, …, B. Goldstein. 2016. Comparative assessment of fluorescent proteins for in vivo imaging in an animal model system. *Mol. Biol. Cell.* 27:3385–3394.

81. Subach, F. V., G. H. Patterson, …, V. V. Verkhusha. 2009. Photoactivatable mCherry for high-resolution two-color fluorescence microscopy. *Nat. Methods.* 6:153–159.

82. Dave, R., D. S. Terry, …, S. C. Blanchard. 2009. Mitigating unwanted photophysical processes for improved single-molecule fluorescence imaging. *Biophys. J.* 96:2371–2381.

83. Bharill, S., C. Chen, …, Y. E. Goldman. 2011. Enhancement of single molecule fluorescence signals by colloidal silver nanoparticles in studies of protein translation. *ACS Nano.* 5:399–407.

84. Glembockyte, V., J. Lin, and G. Cosa. 2016. Improving the photostability of red- and green-emissive single-molecule fluorophores via Ni2+ mediated excited triplet-state quenching. *J. Phys. Chem. B.* 120:11923–11929.

85. Michie, M. S., R. Götz, …, M. J. Schnermann. 2017. Cyanine conformational restraint in the far-red range. *J. Am. Chem. Soc.* 139:12406–12409.

86. Glembockyte, V., R. Wieneke, …, G. Cosa. 2018. Tris -N-nitrilotriacetic acid fluorophore as a self-healing dye for single-molecule fluorescence imaging. *J. Am. Chem. Soc.* 140:11006–11012.

87. Chalfie, M., Y. Tu, …, D. C. Prasher. 1994. Green fluorescent protein as a marker for gene expression. *Science.* 263:802–805.

88. Dickson, R. M., A. B. Cubitt, …, W. E. Moerner. 1997. On/off blinking and switching behaviour of single molecules of green fluorescent protein. *Nature.* 388:355–358.

89. Shaner, N. C., G. H. Patterson, and M. W. Davidson. 2007. Advances in fluorescent protein technology. *J. Cell Sci.* 120:4247–4260.

90. Cranfill, P. J., B. R. Sell, …, D. W. Piston. 2016. Quantitative assessment of fluorescent proteins. *Nat. Methods.* 13:557–562.

91. Ai, H. W., M. A. Baird, …, R. E. Campbell. 2014. Engineering and characterizing monomeric fluorescent proteins for live-cell imaging applications. *Nat. Protoc.* 9:910–928.

92. Thevathasan, J. V., M. Kahnwald, …, J. Ries. 2019. Nuclear pores as versatile reference standards for quantitative superresolution microscopy. *Nat. Methods.* 16:1045–1053.

93. Dunsing, V., M. Luckner, …, S. Chiantia. 2018. Optimal fluorescent protein tags for quantifying protein oligomerization in living cells. *Sci. Rep.* 8:10634.

94. Juette, M. F., D. S. Terry, …, S. C. Blanchard. 2014. The bright future of single-molecule fluorescence imaging. *Curr. Opin. Chem. Biol.* 20:103–111.

95. Zosel, F., A. Holla, and B. Schuler. 2022. Labeling of proteins for single-molecule fluorescence spectroscopy. *In* Protein Folding: Methods and Protocols. V. Muñoz, ed. Springer US, pp. 207–233.

96. Becker, C. F. W., R. Seidel, …, M. Engelhard. 2006. C-terminal fluorescence labeling of proteins for interaction studies on the single-molecule level. *Chembiochem.* 7:891–895.

97. Fernandes, D. D., J. Bamrah, …, C. C. Gradinaru. 2017. Characterization of fluorescein arsenical hairpin (FlAsH) as a probe for single-molecule fluorescence spectroscopy. *Sci. Rep.* 7:13063.

98. Nikić, I., J. H. Kang, …, E. A. Lemke. 2015. Labeling proteins on live mammalian cells using click chemistry. *Nat. Protoc.* 10:780–791.

99. Los, G. V., L. P. Encell, …, K. V. Wood. 2008. HaloTag: a novel protein labeling technology for cell imaging and protein analysis. *ACS Chem. Biol.* 3:373–382.

100. Sun, X., A. Zhang, …, I. R. Corrêa, Jr. 2011. Development of SNAP-tag fluorogenic probes for wash-free fluorescence imaging. *Chembiochem.* 12:2217–2226.

101. Gautier, A., A. Juillerat, …, K. Johnsson. 2008. An engineered protein tag for multiprotein labeling in living cells. *Chem. Biol.* 15:128–136.

102. Blanchard, S. C., R. L. Gonzalez, …, J. D. Puglisi. 2004. tRNA selection and kinetic proofreading in translation. *Nat. Struct. Mol. Biol.* 11:1008–1014.

103. Zhang, M., H. Chang, …, T. Xu. 2012. Rational design of true monomeric and bright photoactivatable fluorescent proteins. *Nat. Methods.* 9:727–729.

104. Jradi, F. M., and L. D. Lavis. 2019. Chemistry of photosensitive fluorophores for single-molecule localization microscopy. *ACS Chem. Biol.* 14:1077–1090.

105. Li, H., and J. C. Vaughan. 2018. Switchable fluorophores for single-molecule localization microscopy. *Chem. Rev.* 118:9412–9454.

106. McEvoy, A. L., H. Hoi, …, R. E. Campbell. 2012. mMaple: a photoconvertible fluorescent protein for use in multiple imaging modalities. *PLoS One.* 7:e51314.

107. Subach, F. V., G. H. Patterson, …, V. V. Verkhusha. 2010. Bright monomeric photoactivatable red fluorescent protein for two-color super-resolution sptPALM of live cells. *J. Am. Chem. Soc.* 132:6481–6491.

108. Dempsey, G. T., J. C. Vaughan, …, X. Zhuang. 2011. Evaluation of fluorophores for optimal performance in localization-based super-resolution imaging. *Nat. Methods.* 8:1027–1036.

109. Grimm, J. B., B. P. English, …, L. D. Lavis. 2015. A general method to improve fluorophores for live-cell and single-molecule microscopy. *Nat. Methods.* 12:244–250.

110. Grimm, J. B., L. Xie, …, L. D. Lavis. 2020. Deuteration improves small-molecule fluorophores. Preprint at bioRxiv. https://doi.org/10.1101/2020.08.17.250027.

111. Nahidiazar, L., A. V. Agronskaia, …, K. Jalink. 2016. Optimizing imaging conditions for demanding multi-color super resolution localization microscopy. *PLoS One.* 11:e0158884.

112. Olivier, N., D. Keller, …, S. Manley. 2013. Resolution doubling in 3D-STORM imaging through improved buffers. *PLoS One.* 8:e69004.

113. van der Velde, J. H. M., J. H. Smit, …, T. Cordes. 2018. Self-healing dyes for super-resolution fluorescence microscopy. *J. Phys. D Appl. Phys.* 52:034001.

114. Tinnefeld, P., and T. Cordes. 2012. "Self-healing" dyes: intramolecular stabilization of organic fluorophores. *Nat. Methods.* 9:426–427. author reply 427-428.

115. Isselstein, M., L. Zhang, …, T. Cordes. 2020. Self-healing dyes—keeping the promise? *J. Phys. Chem. Lett.* 11:4462–4480.

116. Uno, S. N., M. Kamiya, …, Y. Urano. 2014. A spontaneously blinking fluorophore based on intramolecular spirocyclization for live-cell super-resolution imaging. *Nat. Chem.* 6:681–689.

117. Erdmann, R. S., S. W. Baguley, …, D. Toomre. 2019. Labeling strategies matter for super-resolution microscopy: a comparison between HaloTags and SNAP-tags. *Cell Chem. Biol.* 26:584–592.e6.

118. Axelrod, D. 2008. Chapter 7 total internal reflection fluorescence microscopy. *In* Methods in Cell Biology. Academic Press, pp. 169–221.

119. Wu, P.-H., N. Nelson, and Y. Tseng. 2010. A general method for improving spatial resolution by optimization of electron multiplication in CCD imaging. *Opt. Express.* 18:5199–5212.

120. Robbins, M. S., and B. J. Hadwen. 2003. The noise performance of electron multiplying charge-coupled devices. *IEEE Trans. Electron. Devices.* 50:1227–1232.

121. Bigas, M., E. Cabruja, …, J. Salvi. 2006. Review of CMOS image sensors. *Microelectron. J.* 37:433–451.

122. Wang, Y., L. Zhao, …, Z.-L. Huang. 2017. Quantitative performance evaluation of a back-illuminated sCMOS camera with 95% QE for super-resolution localization microscopy. *Cytometry A.* 91:1175–1183.

123. Almada, P., S. Culley, and R. Henriques. 2015. PALM and STORM: into large fields and high-throughput microscopy with sCMOS detectors. *Methods.* 88:109–121.

124. Khaw, I., B. Croop, …, K. Y. Han. 2018. Flat-field illumination for quantitative fluorescence imaging. *Opt. Express.* 26:15276–15288.

125. Lam, J. Y. L., Y. Wu, …, J. S. H. Danial. 2021. An economic, square-shaped flat-field illumination module for TIRF-based super-resolution microscopy. *Biophys. Rep.* https://doi.org/10.1016/j.bpr.2022.100044.

126. Ibrahim, K. A., D. Mahecic, and S. Manley. 2020. Characterization of flat-fielding systems for quantitative microscopy. *Opt. Express.* 28:22036–22048.

127. Herdly, L., P. Janin, …, S. van de Linde. 2021. Tunable wide-field illumination and single-molecule photoswitching with a single MEMS mirror. *ACS Photonics.* 8:2728–2736.

128. Mau, A., K. Friedl, …, S. Lévêque-Fort. 2021. Fast widefield scan provides tunable and uniform illumination optimizing super-resolution microscopy on large fields. *Nat. Commun.* 12:3077.

129. Diekmann, R., K. Till, …, T. Huser. 2017. Characterization of an industry-grade CMOS camera well suited for single molecule localization microscopy – high performance super-resolution at low cost. *Sci. Rep.* 7:14425.

130. Golfetto, O., D. L. Wakefield, …, T. Jovanović-Talisman. 2018. A platform to enhance quantitative single molecule localization microscopy. *J. Am. Chem. Soc.* 140:12785–12797.

131. Zanacchi, F. C., C. Manzo, …, M. Lakadamyali. 2017. A DNA origami platform for quantifying protein copy number in super-resolution. *Nat. Methods.* 14:789–792.

132. Scheckenbach, M., J. Bauer, …, P. Tinnefeld. 2020. DNA origami nanorulers and emerging reference structures. *Apl. Mater.* 8:110902.

133. Lin, R., A. H. Clowsley, …, C. Soeller. 2020. 3D super-resolution microscopy performance and quantitative analysis assessment using DNA-PAINT and DNA origami test samples. *Methods.* 174:56–71.

134. Schmied, J. J., M. Raab, …, P. Tinnefeld. 2014. DNA origami–based standards for quantitative fluorescence microscopy. *Nat. Protoc.* 9:1367–1391.

135. Calebiro, D., F. Rieken, …, M. J. Lohse. 2013. Single-molecule analysis of fluorescently labeled G-protein–coupled receptors reveals complexes with distinct dynamics and organization. *Proc. Natl. Acad. Sci. USA.* 110:743–748.

136. Durisic, N., L. Laparra-Cuervo, …, M. Lakadamyali. 2014. Single-molecule evaluation of fluorescent protein photoactivation efficiency using an in vivo nanotemplate. *Nat. Methods.* 11:156–162.

137. Finan, K., A. Raulf, and M. Heilemann. 2015. A set of homo-oligomeric standards allows accurate protein counting. *Angew. Chem. Int. Ed. Engl.* 54:12049–12052.

138. Chidiac, P., M. A. Green, …, J. W. Wells. 1997. Cardiac muscarinic receptors. Cooperativity as the basis for multiple states of affinity. *Biochemistry.* 36:7361–7379.

139. Li, Y., R. V. Shivnaraine, …, C. C. Gradinaru. 2018. Ligand-induced coupling between oligomers of the M2 receptor and the Gi1 protein in live cells. *Biophys. J.* 115:881–895.

140. Işbilir, A., J. Möller, …, M. J. Lohse. 2020. Advanced fluorescence microscopy reveals disruption of dynamic CXCR4 dimerization by subpocket-specific inverse agonists. *Proc. Natl. Acad. Sci. USA.* 117:29144–29154.

141. Levitz, J., C. Habrian, …, E. Y. Isacoff. 2016. Mechanism of assembly and cooperativity of homomeric and heteromeric metabotropic glutamate receptors. *Neuron.* 92:143–159.

142. Jonas, K. C., F. Fanelli, …, A. C. Hanyaloglu. 2015. Single molecule analysis of functionally asymmetric G protein-coupled receptor (GPCR) oligomers reveals diverse spatial and structural assemblies. *J. Biol. Chem.* 290:3875–3892.

143. Siddig, S., S. Aufmkolk, …, D. Calebiro. 2020. Super-resolution imaging reveals the nanoscale organization of metabotropic glutamate receptors at presynaptic active zones. *Sci. Adv.* 6:eaay7193.

144. Möller, J., A. Isbilir, …, M. J. Lohse. 2020. Single-molecule analysis reveals agonist-specific dimer formation of μ-opioid receptors. *Nat. Chem. Biol.* 16:946–954.

145. Joseph, M. D., E. Tomas Bort, …, S. Simoncelli. 2021. Quantitative super-resolution imaging for the analysis of GPCR oligomerization. *Biomolecules.* 11:1503.

146. He, H., L. Liu, …, F. Huang. 2021. Carbon dot blinking enables accurate molecular counting at nanoscale resolution. *Anal. Chem.* 93:3968–3975.

147. Wisler, J. W., K. Xiao, …, R. J. Lefkowitz. 2014. Recent developments in biased agonism. *Curr. Opin. Cell Biol.* 27:18–24.